J. Phys. B: At. Mol. Opt. Phys. **42** (2009) 085301 (8pp) doi:10.1088/0953-4075/42/8/085301

Fabricating atom chips with femtosecond laser ablation

C H Wolff, S Whitlock, R M Lowe, A I Sidorov and B V Hall

ARC Centre of Excellence for Quantum-Atom Optics and Centre for Atom Optics and Ultrafast Spectroscopy, Swinburne University of Technology, Hawthorn, Victoria 3122, Australia

E-mail: brhall@swin.edu.au

Received 3 February 2009
Published 9 April 2009
Online at stacks.iop.org/JPhysB/42/085301

Abstract

We report on the microfabrication of atom chips using a femtosecond laser ablation technique to arbitrarily sculpture both thin conductive metal films and permanent magnetic materials. We have measured the threshold fluences for a variety of materials relevant to atom chip development (Au, Ag, Cu, Cr, Ni, TbGdFeCo, SmCo, CoCr). The quality of the ablation process is investigated by extracting the power spectral density of the edge roughness from composite scanning electron microscope images and through the use of a magnetoresistance microscope to measure the associated magnetic field noise. Finally, we present results from a sculptured wire which produces an array of tunable double wells designed for near-surface force sensing with Bose–Einstein condensates.

(Some figures in this article are in colour only in the electronic version)

1. Introduction

The atom chip area of research which exploits surface-based potentials to manipulate cold quantum gases on the micron scale has attracted widespread interest in recent years with several excellent review articles [1–3] and a textbook on the topic in print [4]. The workhorse components of atom chips are either planar geometries of microfabricated wires [5–9] or patterned magnetic materials [10–12], and it is these components which provide the intricate magnetic potentials that enable practical and robust tools for producing, trapping and manipulating Bose–Einstein condensates (BECs). Conventional methods for fabricating atom chips typically involve several steps including e-beam lithography to produce high resolution photo-masks, ultraviolet photolithography and wet etching. These methods can be costly and time-consuming processes which often require proprietary industry expertise. As a promising alternative, femtosecond laser ablation can be performed in virtually any laboratory to pattern a wide variety of materials with submicron resolution. Notably the thermal damage surrounding the ablation point is significantly reduced for femtosecond pulses yielding a superior finish when compared to picosecond or nanosecond schemes [14]. Thus, this method allows complex quality micromachining of conductors and magnetic materials to produce atom chips. Further advantages include the ability to drill holes and cut grooves with extremely high aspect ratios [13], yield thick wires for large currents or sculpt the atom chip surface [15].

In this paper, we describe the microfabrication of atom chip elements using femtosecond laser ablation techniques. A variety of materials that are of interest for the atom chips is studied, and we report the threshold laser fluence required to successfully remove film thicknesses in the range 100–300 nm. The quality of the laser ablation is investigated for current carrying wires crafted in evaporatively deposited copper. The power spectral density (PSD) of the edge roughness gives a quantitative measure of the quality of this technique and allows direct comparisons with other fabrication technologies. In addition, we utilize magnetoresistance microscopy to directly measure the magnetic field above a sculptured microwire with results juxtaposed to finite element analysis calculations. This sculptured geometry is used to motivate experiments that adiabatically split a BEC in a double well above a structured surface, to realize a sensitive measurement device for near-surface forces.

2. Ablation apparatus and procedure

A schematic of the apparatus is shown in figure 1. The femtosecond laser system consists of a mode-locked Ti:sapphire laser (Tsunami, Spectra Physics) and

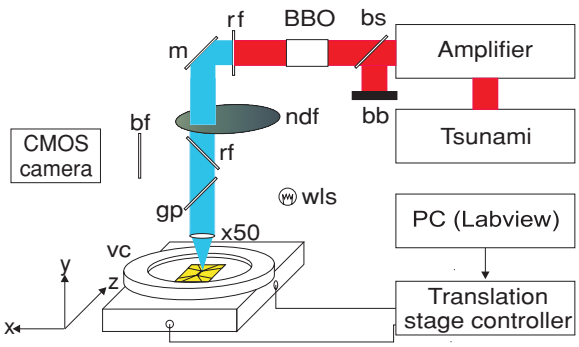

Figure 1. Schematic diagram of the laser ablation apparatus. Abbreviations: bs, beam splitter; bb, beam block; BBO, BBO crystal; rf, red filter; m, mirror; ndf, neutral density filter; gp, glass plate; wls, white light source; bf, blue filter; vc, vacuum chamber.

a regenerative amplifier (Spitfire, Spectra Physics) which delivers 80 fs, 1 mJ laser pulses at a centre wavelength of 800 nm and a repetition rate of 1 kHz. Upon exiting the regenerative amplifier, the beam is frequency doubled using a second harmonic generating crystal beta-BaB_2O_4 (BBO). A 400 nm beam passes a red optical filter and a neutral density wheel which allows the average laser power to be continuously varied between 0 and 500 μW. The beam transits a high numerical aperture (NA = 0.5) Olympus LMPlanFL × 50 microscope objective lens which is mounted on a vertical micrometer-screw-controlled stage. The working distance of this lens system is 10 mm with a measured 0.7 μm beam waist at the focal plane, yielding a depth of focus of 8 μm as determined by the Rayleigh length. In addition to the smaller beam waist achievable with the 400 nm light, we also observe less thermal damage and an improved edge quality of ablated grooves on metal films.

The sample is placed in a home-built vacuum chamber with a 50 mm diameter fused silica viewport for optical access. The chamber is pumped with a 0.5 L s^{-1} two-stage rotary pump producing a vacuum of 10 mTorr. This vacuum dramatically reduces the amount of debris produced during ablation since the mean free path for ejected material is much greater than the chamber dimensions [14]. In addition to the laser beam, we focus a white light source through the objective lens to illuminate the sample. The back-reflected light is then imaged to a CMOS camera to monitor the patterned area of the surface during ablation. The vacuum system and sample are clamped to a two-dimensional positioning system. This consists of two orthogonal, computer-controlled stepper-motor-operated Newport translation stages (UTM150PP.1) interfaced to a standard desktop PC under Labview control. The stages have a resolution of 100 nm, a maximum travel distance of 150 mm and a maximum translation speed of 2 mm s^{-1}. This range of motion is considerably greater than our atom chip dimensions, typically 25 × 25 mm^2, thus allowing microfabrication in a single writing process.

Prior to writing the chip pattern, the surface to be ablated must be made parallel to the plane of translation. Alignment is achieved by maintaining a focused image of the chip surface (CMOS camera, figure 1) during x–z translation. Using this method, a 16 × 16 mm^2 region can be patterned with low power as it remains within the Rayleigh range of the focused laser pulse. Outside this region, the laser power is increased for complete ablation. This procedure circumvents the need for active control of the objective–surface separation. In addition, we observed that the focal plane for white light was 7 μm beneath that for the 400 nm ablation pulse. This constant offset was determined by observing the onset of ablation as a function of objective–surface separation. This offset is a function of the imaging optics and the illumination process and is a constant of the apparatus set-up, being independent of the sample to be ablated.

3. Determination of thin film threshold fluences

Before undertaking the fabrication of an atom chip, the effect of laser intensity upon the width of the ablated groove was investigated for a variety of materials of interest. These materials can be broadly grouped into three ranges: high conductivity transition metals (Au, Ag, Cu) typically used as conductive wire elements, low conductivity transition metals (Cr, Ni) used to enhance metal–substrate bonding and permanent magnetic alloys (TbGdFeCo, SmCo, CoCr) for recently developed permanent magnet atom chips [11]. For this study, a series of equally spaced grooves were ablated in a given material with successively increasing laser powers. The grooves were cut with a constant translation speed of 0.2 mm s^{-1} with a pulse repetition rate of 1 kHz. Thus each laser pulse is spatially separated by 0.2 μm, approximately one-quarter of the beam waist. The result of one such process is presented in figure 2(b) which shows an image of the ablated grooves taken with an optical microscope in a transmission mode. To extract the threshold ablation fluence (Φ_{th}) and the laser spot size (w_0), we use an adaptation of a previous investigative method reported in [16, 17] in which the ablation morphology of a crater was studied and the crater diameter was found to be logarithmically dependent upon the laser fluence. For the thin material investigated here, the lateral width of the ablated grooves serves as a one-dimensional analogue where the spatial fluence profile $\Phi(r)$ is for a Gaussian beam given by

$$\Phi(r) = \Phi_0 \exp\left[\frac{-2r^2}{w_0^2}\right], \tag{1}$$

where r is the distance from the beam centre, Φ_0 denotes the maximum laser fluence at the cross-sectional surface and w_0 is the $1/e^2$ width of the focused laser beam. The maximum fluence and the pulse energy E_{pulse} are thus related by

$$\Phi_0 = \frac{2E_{pulse}}{\pi w_0^2}. \tag{2}$$

Defining the groove diameter as $2r$ yields

$$D^2 = 2w_0^2\left[\ln(E_{pulse}) + \ln\left(\frac{2}{\pi w_0^2 \Phi_{th}}\right)\right]. \tag{3}$$

Plotting D^2 versus $\ln(E_{pulse})$ yields a straight line function with the slope equivalent to the spot size and x-intercept returning the threshold fluence Φ_{th}. This behaviour is evident in figure 2(a) where the widths of the ablated grooves have been extracted from the Gaussian fits of the optical image data

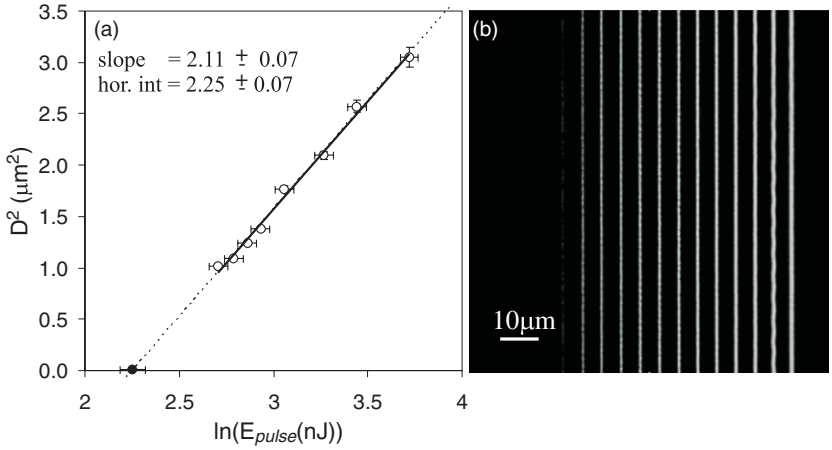

Figure 2. (a) Squared diameter D^2 of the ablated lines in 100 nm thick Cr versus the natural logarithm of the pulse energy. The data points (open circles) and errors are obtained using nonlinear regression to fit the Gaussian profiles to the ablated channels imaged using a microscope in a transmission mode, shown in (b). To characterize the ablation process for each material, the minimum beam width w_0 and the threshold fluence Φ_{th} are extracted from the straight line fit of equation (3).

Table 1. Threshold fluences Φ_{th} for various materials which are laser ablated under vacuum with 400 nm, 80 fs pulses. Materials of interest for atom chips include the high conductivity metals (Au, Ag, Cu), bonding metals (Ni, Cr) and permanent magnet alloys (TbGdFeCo, CoCr, SmCo).

Material	Φ_{th} (J cm^{-2})	±
Silver	1.77	0.35
Nickel	0.98	0.26
TbGdFeCo	0.69	0.03
SmCo	0.65	0.28
Copper	0.64	0.12
Chromium	0.58	0.08
CoCr	0.57	0.20
Gold	0.41	0.09

and their square has been plotted against the natural logarithm of the peak pulse energy. These results are for a 100 nm thin film coating of chromium which is typically used as an intermediate bonding material for noble metals (Au and Ag) and for magnetic alloys (TbGdFeCo). Similar procedures were followed for a variety of materials with their threshold fluences tabulated in table 1. We note that in the literature, an often quoted material property is the threshold laser fluence for surface damage which represents the onset of localized laser-induced melting [18]. In this paper, we have focused on the maximum removal of a substantial thickness of material per pulse which may be more relevant in simplifying the atom chip fabrication process. Larger ablation depths can be acquired via multiple pulses on the same position, for example, by driving the translation stage more slowly or by using a multiple raster technique, since the removal of material is linearly dependent on the pulse number [17].

4. Edge quality characterization with scanning electron microscopy

While the ablation of insulating grooves underpins the atom chip fabrication technique (section 2), the resulting microscopic wire quality which determines the degree of *fragmentation* induced by the method is of principle importance. Fragmentation is an unexpectedly striking but deleterious effect which causes ultracold gases or BECs to break into lumps near a wire. Fragmentation occurs when corrugations in the magnetic trapping potential [19, 20] become comparable in magnitude to the thermal energy/chemical potential of a cold cloud/BEC. These corrugations in the magnetic potential are caused by small meanderings of the current which have resulted from imperfect, rough edges of the atom chip wires [7, 21]. Fragmentation has also been observed above permanently magnetized thin film atom chips being attributed to small magnetic inhomogeneities rather than edge roughness [22]. While it was recently reported that kHz frequency modulation of the field currents can be used to smooth out corrugations that would exist in a dc-current trap [23, 24], substantial effort has also been invested in the implementation of higher quality lithographic fabrication to reduce the wire edge and surface roughness [9].

To initially investigate the edge quality, the ablated wires were imaged using a Zeiss SUPRA Field emission scanning electron microscope (SEM) with a magnification of $\times$12 500. Two such images are shown in figure 3 with (a) yielding qualitative information about the debris field resulting from ablation close to and far above threshold. Figure 3(b) highlights both the round-off curvature that is encountered when nano-sculpting a wire and the intricate dual layer ablation pattern that arises due to the slightly different threshold fluences of the top reflective gold which was deposited on the copper conductor.

To extract the edge roughness of a straight ablated wire, 42 SEM images were taken as the wire was translated within the microscope. By manually combining the images in software, a single composite picture of a 640 μm long wire was produced. An edge finding algorithm was then employed to find the position of the copper edge for each of the 40 000 pixel columns by using the brightness change between the pixels. A

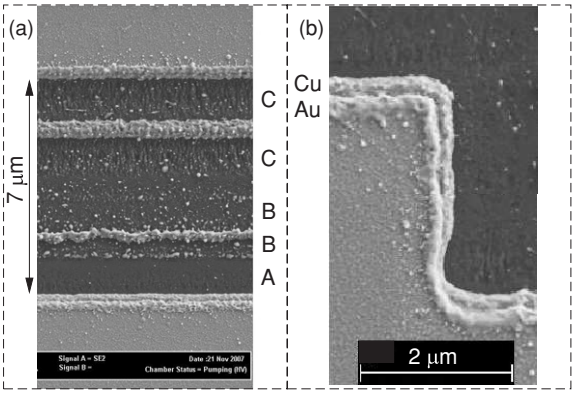

Figure 3. Scanning electron microscope images taken of the ablated surface for both straight and sculptured wires. (a) Row A shows clean debris-free ablation achieved by using two successive cuts at a 55 nJ pulse energy. Row B is a single cut with this power. Row C shows above threshold ablation at 144 nJ yielding significant debris and substrate damage. (b) SEM image of a sculptured wire. The two ablation thresholds of the overlying gold and the underlying copper are evident as the lower threshold Au can be seen to ablate further from the wire edge in the low intensity wings of the laser spot.

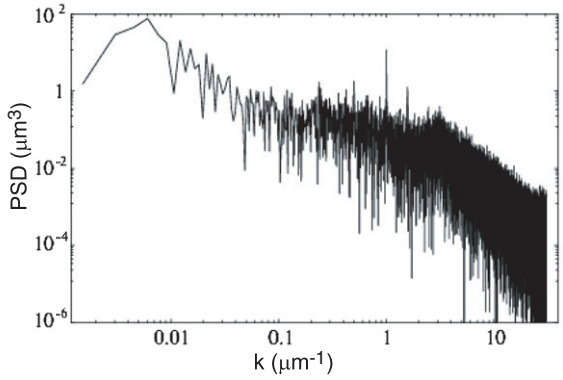

Figure 4. Power spectral density of the edge fluctuations plotted as a function of the wavevector k which is inversely related to the wavelength of the spatial fluctuation. These data are extracted from a series of high resolution SEM images that were stitched together using post-processing methods. Integration over k yields the RMS width of the edge noise $\delta x_{\mathrm{RMS}} = 16$ nm. The absence of large peaks in the PSD implies that there are no dominant corrugation periods arising from the ablation process.

straight line fit to the edge position allowed the edge deviation from this fit to be calculated in each pixel column. The RMS width of the edge fluctuations δx_{RMS} was then calculated from these data to be 16 nm. This compares very favourably to a similar investigation of the edge roughness of electroplated microwires where a RMS edge roughness of 200 nm was measured [7]. In addition to the edge roughness, figure 3(b) also shows a localized top surface deformation which extends into the wire approximately 200 nm from the edge. It has been shown that surface roughness on the top of microwires has a significantly smaller corrugating influence on the magnetic potential [21]. For the ablated wires, this should be even further suppressed as this surface roughness only occurs for a small percentage of the top wire surface (<2% assuming a wire width of 25 μm).

While the SEM allows a rapid measurement of δx_{RMS}, substantially more information is available when the PSD of the edge fluctuations is extracted via a discrete Fourier transform of the spatial information held within the composite image. A Fourier transform was performed numerically with the results plotted in figure 4. The spatial fluctuation wavevector k spans four orders of magnitude along the horizontal axis with the sparsity of the leftmost points indicating that the fluctuation wavelength approaches the size of the image (650 μm $\rightarrow$ $k \approx 0.01$) and the densely represented rightmost points which truncate at the pixel size. Importantly, there are no peaks within this spectrum especially at long spatial wavelengths which we attribute to the careful implementation of high performance stepper-motor-controlled translation stages in combination with securely mounted optics on low vibration 1″ posts. We note that these results were also achieved with the lasers and ablation apparatus mounted on two separate, decoupled, non-floating vibration-isolating optical tables.

5. Magnetoresistance microscopy of a straight wire

While the SEM images provide some qualitative information about the ablated edge quality, a direct measure of the magnetic potential created by a flowing current is required as this is ultimately what the quantum gas experiences. Ultracold atoms have recently been demonstrated as highly sensitive field probes perhaps heralding a new form of cold-atom microscopy [8]. A complementary solid-state technique that can quickly be performed in atmosphere was recently demonstrated in our laboratory based on a microscopic (5×5 μm^2 active area) magnetic tunnelling junction sensor (MicroMagnetics STJ-020), which measures the out-of-plane B_y magnetic field component above either microwires or permanent magnetic media [25]. Briefly, the microscope consists of the MR sensor probe, preamplification electronics, a lock-in amplifier (LIA), UTM150PP.1 translation stages for x and z positioning and a computer control. The probe tip is manually positioned above the sample using a micrometer stage and a CMOS camera for height calibration. The whole system is mounted on an optical table for vibration isolation. With this set-up, both one-dimensional scans and two-dimensional maps of B_y can be acquired at various heights above the sample surface.

MR microscopy of the ablated wire begins with a one-dimensional scan at a fixed height by translating the chip beneath the stationary probe in the x-direction. A 1.7 kHz ac current of 70 mA sourced by the LIA is run through a 100 μm wide ablated wire, and the resulting MR-sensor signal which is modulated at this frequency is isolated and integrated for 100 ms within the same LIA. A Labview program records the LIA output while controlling the stage translation which is not continuous but stepwise, with 5 μm increments, translated over 50 ms with a 500 ms dwell time to ensure the independence of the LIA integration process. With this technique, the RMS noise level is reduced to about 0.1 μT equivalent to that obtained using ultracold atoms as a probe [22]. From this process, a dispersion-shaped curve for B_y is extracted which

in the approximation of an infinitely thin wire can be fitted with the following expression:

$$B_y = \frac{\mu_0 I}{2\pi\sqrt{(x-x_0)^2+h^2}} \sin\left[\arctan\left(\frac{x-x_0}{h}+\alpha\right)\right], \quad (4)$$

where x_0 is the position of the wire centre, h is the height of the sensor above the wire, I is the wire current, μ_0 is the permeability of free space and α is the angle between the sensor and the normal to the chip surface. This expression is appropriate in the y-direction as the 500 nm wire thickness is small compared to the typical closest approach distance >20 μm. In the scanned x-direction, the wire width is 100 μm which is comparable to the closest approach distance; however, it is still small compared to the total distance that is scanned in x, typically ± 1 mm either side of the wire. As such, (4) can still be fitted to the measured one-dimensional scans to establish the probe–surface separation to an accuracy better than that obtained from the micrometre scale which manually controls the probe height.

To acquire a two-dimensional map of B_y, the above process is repeated with a 5 μm resolution step in the z-direction. This map at a fixed height can be converted to a uniquely defined in-plane current distribution and subsequently back to any other field component provided the wire height is small compared to the measurement distance above the surface and the current density can be considered as a two-dimensional distribution, two conditions fulfilled by our thin ablated wire [26, 25]. Using this method, a two-dimensional map of B_x and B_z were numerically extracted from the measured B_y data. For ultracold atoms trapped above this ablated wire, the corrugating potential of interest is defined by the spatial fluctuations in the field component B_z measured directly above and along the wire centre. This component is commonly called $B_\parallel$ referring to the fact that it is the field component that is parallel to the wire direction. Figure 5 shows the spatial variation of $B_\parallel$ recorded at a height of 60 μm above the wire. From these data the root mean square for the variation in $B_\parallel$ can be calculated as $B_{\parallel\mathrm{RMS}} = 1.8 \times 10^{-7}$ T which is then used to establish another figure of merit $B_{\parallel\mathrm{RMS}}/B_\perp$, where $B_\perp$ is equivalent to B_x directly above the wire centre at the height of interest. This figure of merit is useful as it is independent of the current through the wire with smaller values indicating less corrugation. In this measurement $B_\perp = 2.4 \times 10^{-4}$ T, yielding $B_{\parallel\mathrm{RMS}}/B_\perp = 7.5 \times 10^{-4}$ for a height of 60 μm. In a recent paper [9], the authors collated $B_{\parallel\mathrm{RMS}}/B_\perp$ results for a broad range of fabrication methods and from first appearances the above result indicates that the ablation method is most closely comparable to that reported by the Tübingen group [27].

Upon closer inspection of figure 5, it appears that the spatial variation of $B_\parallel$ is largest for periods approaching the 5 μm step size. At the measurement height of 60 μm, these fluctuations are unlikely to be due to real wire edge roughness as the Fourier field components decay rapidly from the wire with a characteristic length comparable to the period of corrugation [21, 28]. We interpret this behaviour as an indication that the femtosecond ablated wire has a roughness which is below the noise floor of the MR microscope. This motivates a future exploration of the ablated atom chip where a BEC will provide more sensitive measurement.

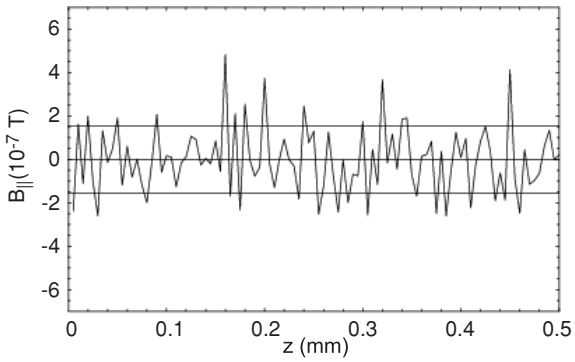

Figure 5. Magnetoresistance microscopy performed at a height of 60 μm above an ablated wire allows the magnetic field component $B_\parallel$ to be extracted as a function of the distance along the wire. The root mean squared value of $B_\parallel$ was 1.8×10^{-7} T, as indicated by the horizontal lines about zero.

6. Magnetoresistance microscopy of a sculptured wire

While fragmentation is typically reported as a deleterious effect, recent experiments in our laboratory show that the controlled spitting of a BEC from a single to a double-well potential along the axial direction provides a sensitive probe for forces which induce an asymmetry in the double well [29]. In this realization, the corrugated potential was fortuitously provided by random magnetic inhomogeneity; however, a more controlled approach was desired. The design and lithographic fabrication of patterned microwires to produce complex magnetic potentials for ultracold atom experiments have been described in the literature [15]; however, here we report on deliberate sculpturing of a wire with femtosecond laser ablation. To produce an array of microscopic magnetic traps which can be controllably split into an array of symmetric double-well potentials relies on sculpting two dominant spatial waveforms with different periods (one long Λ and one short λ) into either edge of a straight microwire (figure 6(a)). Each waveform gives rise to a corrugation in the magnetic potential whose spatial period is associated with the sculptured waveforms; however, the λ period corrugation decays more rapidly with the distance from the wire than the Λ period corrugation. BEC splitting is achieved by increasing the magnitude of a homogeneous bias field B_x that shifts the microwire trap towards the wire, increasing the strength of the λ period corrugation.

To reduce the patterning complexity rather than sinusoidal functions, two square wave edge waveforms, $\lambda = 100$ μm and $\Lambda = 300$ μm, were chosen with peak-to-peak amplitudes of 10 μm and 3.2 μm, respectively. While this results in additional higher frequency odd order Fourier components in the PSD, the majority of the power (81%) resides in the first term with further (9%) in the next non-zero term. As the waveforms are phase locked such that outward steps are coincident, higher order terms have a negligible contribution at the heights of interest. Prior to fabrication, this structure was computationally modelled using finite element analysis

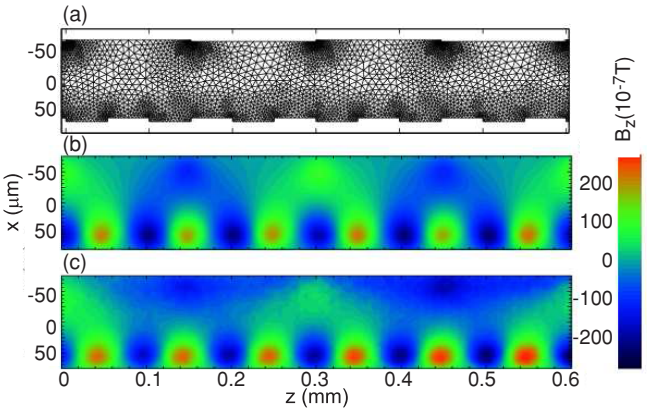

Figure 6. Comparison of the magnetic field topology above a sculptured wire. (a) Finite element analysis mesh indicating the dual edge fabrication pattern, (b) numerical simulation of the B_z magnetic field component evaluated at a height of 17 μm above the wire for 150 mA current and (c) experimental map of B_z produced using the MR microscope to map the field above the laser ablated sculptured wire.

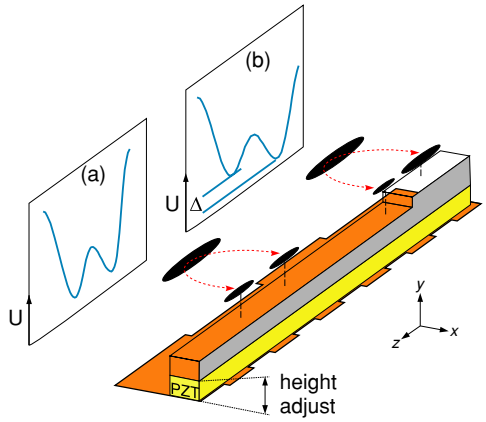

Figure 7. Schematic of an adiabatic splitting experiment that uses the sculpture wire pattern of figure 6. In (a), the attractive C–P potential is both balanced and strongly attenuated due to the increasing distance between the dw potential and the surface under study. In (b), the right well is lowered by the attractive C–P potential due to the close proximity of the raised surface. This results in a larger condensate fraction in the right well. The height of the structured surface is controllable at the nanometre level by a piezo-electric disk.

routines in Matlab to solve for the current distribution resulting from the sculptured wire (figure 6(a)). A two-dimensional map of B_z at a height of 17 μm is numerically evaluated (figure 6(b)). The dual period corrugation is clearly evident and, in the presence of a small offset field ($B_{\text{off}} = 1 \times 10^{-4}$ T), localized field minima occur, shown in a false colour (blue). From this image, an additional mechanism for trap splitting can also be observed where the trap is held at a fixed height and is horizontally translated across the wire width. These theoretical results show good agreement with the MR-microscope measurements of the real ablated wire (figure 6(c)). While a small asymmetry, typically less than 5% of the barrier height, is present in the array of double-well potentials, it is sufficiently small to motivate a BEC sensor experiment to measure the attractive Casimir–Polder (C–P) force.

7. Sensing near-surface forces

In 1948, Casimir and Polder investigated the effect of retardation on the short-range, attractive London–van der Waals force between a neutral atom and a perfectly conductive wall [30]. They found a monotonically decreasing correction factor, which approaches unity for $y \ll \lambda/2\pi$ and scales as y^{-1} for $y \geqslant \lambda/2\pi$ where y is the atom–wall separation and $\lambda/2\pi$ is the distance associated with the wavelengths λ corresponding to possible transition energies of the atom. In this region, the Casimir–Polder potential is

$$U(y) = -\frac{3}{8\pi}\hbar c\alpha(0)y^{-4}, \tag{5}$$

where $\alpha(0)$ is the static polarizability of the atom. This interaction is a direct result of the electromagnetic vacuum whose interest has motivated numerous theoretical extensions to equation (5) to account for real world effects, such as material composition, geometry and finite temperature [31]. In addition, recent precision measurement techniques using the BEC as a probe have enabled this interaction to be investigated quantitatively [32–34]. A schematic representation of the proposed experiment is shown in figure 7 which uses an atom chip with a central conductive wire sculptured in the pattern indicated (figure 6). Initially, ultracold ^{87}Rb atoms are trapped in the $F = 1$, $m_F = -1$ state and evaporatively cooled to a BEC using the long-period axial array that is localized on the left-hand side of the wire at a height of $\approx$100 μm. For a 300 mA wire current which is sustainable for microwires [35], the typical radial trap frequency $\omega_r/2\pi = 220$ Hz where the offset field is chosen as $B_z = 3.2 \times 10^{-4}$ T. For the 300 μm long period, the axial trap frequency is $\omega_z/2\pi = 28$ Hz. With each well in the array containing 10^4 condensed atoms, the chemical potential $\mu = 910$ Hz.

Since the condensate only samples a restricted fraction of the B_z landscape, it is straightforward to adiabatically transport it horizontally across the wire transforming the axial confinement from a single well into a double-well potential. In figure 7 this double well is localized above the short period, right side of the wire edge. At this edge, a structured sapphire surface is introduced whose height is controllable with a piezo-electric transducer. In section (a), the surface is uniformly flat in addition to being recessed by 20 μm when compared to the surface below section (b). This recessed section attenuates the C–P potential such that its effect is unobservable thus making (a) a calibration sensor which enables non-C–P effects to be corrected for, for example a slow drift in the magnetic field gradient along z over time. The half-raised section above (b) introduces a spatially localized C–P effect which introduces an asymmetry in the double-well potential.

The magnitude of this asymmetry is dependent upon the distance between the surface and the trapping minimum and can be calculated using established parameters for alkali

atoms such as ^{87}Rb [36]; for example, at 1 μm separation an asymmetry of $\Delta/2\pi = 3$ Hz develops. This level of asymmetry should be discernable with just a single measurement using the adiabatic splitting technique given the above parameters and shot-noise-limited atom detection capability. This can be further improved with averaging over multiple measurements provided statistical fluctuations dominate. Moreover in a recent paper, it was theoretically shown that a phase separable two-component BEC could be used to improve the mapping accuracy for potential energy landscapes over that performed with a single BEC [37]. This improvement requires that the scattering parameters are comparable and that both BEC components experience essentially the same potential landscape. Both of these criteria are met using the $F = 1$, $m_F = -1$ and $F = 2$, $m_F = 1$ states in ^{87}Rb which can be easily prepared using a two-photon microwave plus radio frequency transition [38]. The chemical potential of a single condensate sets the accessible energy scale of the splitting measurement and cannot be arbitrarily lowered without reducing the density and the atom imaging signal. A better strategy is to adopt a two-component system where the effective potential that the components experience is scaled by $1 - \left(\frac{a_{11}}{a_{22}}\right)^{1/2}$, where a_{11} and a_{22} are the interstate scattering amplitudes. Using ^{87}Rb parameters, a possible 35$\times$ improvement in sensitivity motivates future exploration of this concept.

8. Conclusion

We have demonstrated that femtosecond laser ablation can be used as an effective fabrication technique for the realization of microwire-based atom chips that are patterned with nanoscale resolution. We have measured the ablation threshold fluence for a variety of conductive metals and magnetic films that are used for atom chip experiments. The edge quality of a microwire produced using this fabrication method was investigated using scanning electron microscopy and magnetoresistance microscopy. The SEM results revealed an RMS edge roughness, an order of magnitude smaller than those reported for lithographic wires which had been enhanced with electroplating. The magnetic field potential roughness above the ablated wire was evidenced to be below the noise floor of the MR microscope motivating a future investigation with low energy Bose–Einstein condensates. In addition, a sculptured wire was realized which enables the production of an array of highly symmetric axial double wells for possible BEC sensor experiments. One such experiment for a direct measurement of the Casimir–Polder potential close to a surface was elucidated using the sculptured wire potential.

Acknowledgments

We thank H Brinkies for his assistance in capturing the SEM images and Dr J Wang for the thin film deposition. This project is supported by the ARC Centre of Excellence for Quantum-Atom Optics.

References

[1] Hinds E A and Hughes I G 1999 *J. Phys. D: Appl. Phys.* **32** R119
[2] Folman R, Krüger P, Schmiedmayer J, Denschlag J and Henkel C 2002 *Adv. At. Mol. Opt. Phys.* **42** 263
[3] Fortágh J and Zimmermann C 2007 *Rev. Mod. Phys.* **79** 235
[4] Reichel J and Vuletic V 2009 *Atom Chips* (New York: Wiley) in preparation
[5] Hänsel W, Hommelhoff P, Hänsch T W and Reichel J 2001 *Nature* **413** 498
[6] Jones M P A, Vale C J, Sahagun D, Hall B V and Hinds E A 2003 *Phys. Rev. Lett.* **91** 080401
[7] Estève J, Aussibal C, Schumm T, Figl C, Mailly D, Bouchoule I, Westbrook C I and Aspect A 2004 *Phys. Rev.* A **70** 043629
[8] Schumm T, Hofferberth S, Andersson L M, Wildermuth S, Groth S, Bar-Joseph I, Schmiedmayer J and Krüger P 2005 *Nature* **1** 57
[9] Krüger P, Andersson L M, Wildermuth S, Hofferberth S, Haller E, Aigner S, Groth S, Bar-Joseph I and Schmiedmayer J 2007 *Phys. Rev.* A **76** 063621
[10] Sinclair C D J, Curtis E A, Llorente-Garcia I, Retter J A, Hall B V, Eriksson S, Sauer B E and Hinds E A 2005 *Phys. Rev.* A **19** 74
[11] Hall B V, Whitlock S, Scharnberg F, Hannaford P and Sidorov A 2006 *J. Phys. B: At. Mol. Opt. Phys.* **39** 27
[12] Fernholz T, Gerritsma R, Whitlock S, Barb I and Spreeuw R J C 2008 *Phys. Rev.* A **77** 033409
[13] Zhang Y, Lowe R M, Harvey E, Hannaford P and Ends A 2002 *Appl. Surf. Sci.* **186** 345
[14] Preuss S, Demchuk A and Stuke M 1995 *Appl. Phys.* A **61** 33
[15] Pietra L D, Aigner S, Hagen C V, Lezec H J and Schmiedmayer J 2005 *J. Phys.: Conf. Ser.* **19** 30
[16] Liu J M 1982 *Opt. Lett.* **7** 196
[17] Bonse J, Wrobel J M, Krügger J and Kautek W 2001 *Appl. Phys.* A **72** 89
[18] Wellershoff S S, Hohlfeld J, Güdde J and Matthias E 1999 *Appl. Phys.* A **69** S99
[19] Kraft S, Gunther A, Ott H, Wharam D, Zimmermann C and Fortagh J 2002 *J. Phys. B: At. Mol. Opt. Phys.* **35** L429
[20] Leanhardt A E, Shin Y, Chikkatur A P, Kielpinski D, Ketterle W and Pritchard D E 2003 *Phys. Rev. Lett.* **90** 100404
[21] Wang D W, Lukin M D and Demler E 2004 *Phys. Rev. Lett.* **92** 076802
[22] Whitlock S, Hall B V, Roach T, Anderson R, Volk M, Hannaford P and Sidorov A I 2007 *Phys. Rev.* A **75** 043602
[23] Trebbia J B, Alzar C L G, Cornelussen R, Westbrook C I and Bouchoule I 2007 *Phys. Rev. Lett.* **98** 263201
[24] Bouchoule I, Trebbia J B and Alzar C L G 2008 *Phys. Rev.* A **77** 023624
[25] Volk M, Whitlock S, Wolff C H, Hall B V and Sidorov A I 2008 *Rev. Sci. Instrum.* **79** 023702
[26] Roth B J, Sepulveda N G and Wilkswo J P 1989 *J. Appl. Phys.* **65** 361
[27] Fortagh J 2003 *PhD Thesis* Universität Tübingen
[28] Schumm T, Estève F, Trebbia J B, Aussibal C, Nguyen H, Mailly D, Bouchoule I, Westbrook C I and Aspect A 2005 *Eur. Phys. J.* D **32** 171
[29] Hall B V, Whitlock S, Anderson R, Hannaford P and Sidorov A I 2007 *Phys. Rev. Lett.* **98** 030402
[30] Casimir H B G and Polder D 1948 *Phys. Rev.* **73** 360–72
[31] Babb J K 2005 *J. Phys: Conf. Ser.* **19** 1 (and references therein)
[32] Pasquini T A, Shin Y, Sanner C, Saba M, Schirotzek A, Pritchard D E and Ketterle W 2005 *Phys. Rev. Lett.* **93** 223201

[33] Harber D M, Obrecht J M, McGuirk J M and Cornell E A 2005 *Phys. Rev.* A **72** 033610
[34] Obrecht J M, Wild R J, Antezza M, Pitaevskii L P, Stringari S and Cornell E A 2007 *Phys. Rev. Lett.* **98** 063201
[35] Groth S, Krger P, Wildermuth S, Folman R, Fernholz T, Schmiedmayer J, Mahalu D and Bar-Joseph I 2004 *Appl. Phys. Lett.* **85** 2980
[36] Antezza M, Pitaevskii L P and Stringari S 2004 *Phys. Rev.* A **70** 053619
[37] Bhongale S G and Timmermans E 2008 *Phys. Rev. Lett.* **100** 185301
[38] Matthews M R, Hall D S, Jin D S, Ensher J R, Wieman C E, Cornell E A, Dalfovo F, Minniti C and Stringari S 1998 *Phys. Rev. Lett.* **81** 243